Supplementary Materials for:

Hippocampal subfields and limbic white matter jointly predict learning rate in older adults

Andrew R. Bender,
Department Epidemiology and Biostatistics and Department of Neurology and Ophthalmology, Michigan State University, East Lansing, MI, USA
Center for Lifespan Psychology, Max Planck Institute for Human Development, Berlin, Germany

Andreas M. Brandmaier,
Center for Lifespan Psychology, Max Planck Institute for Human Development, & Max Planck UCL Centre for Computational Psychiatry and Ageing Research, Berlin, Germany and London, UK,

Sandra Düzel,
Center for Lifespan Psychology, Max Planck Institute for Human Development, Berlin, Germany

Attila Keresztes,
Center for Lifespan Psychology, Max Planck Institute for Human Development, Berlin, Germany
Research Centre for Natural Sciences, Hungarian Academy of Sciences, Budapest, Hungary, Faculty of Education and Psychology, Eotvos Lorand University, Budapest, Hungary

Ofer Pasternak
Departments of Psychiatry and Radiology, Brigham and Women's Hospital, Harvard Medical School, Boston, MA, USA

Ulman Lindenberger
Center for Lifespan Psychology, Max Planck Institute for Human Development, & Max Planck UCL Centre for Computational Psychiatry and Ageing Research, Berlin, Germany, and European University Institute, San Domenico di Fiesole (FI), Italy

Simone Kühn
Center for Lifespan Psychology, Max Planck Institute for Human Development, &
Department of Psychiatry and Psychotherapy, University Clinic Hamburg-Eppendorf, Hamburg, Germany

Supplementary Materials

Methods

ROI creation. Three regions were used to specify inclusion of fornices: a seed mask was placed in the coronal plane on the body of the fornix and transverse-oriented inclusion masks were drawn at the level of mammillary bodies and, and bilateral masks were drawn on the coronal plane at crus of the fornix, one just posterior hippocampal body and one more superior. Exclusion masks were drawn 1) on the coronal plane, two slices anterior to the fornix, 2) on the coronal plane, in the splenium of the corpus callous (CC), and 3) anterior to the columns of the fornix, and 4) inferior to the mammillary bodies. The CBD was defined by a single seed ROI placed in the middle of the dorsal cingulum, with regions of inclusion and termination anterior to the genu of the CC and posterior to the CC splenium. Exclusion masks were liberally placed dorsal, rostral, and caudal to the CBD to limit the tract to its core projections. A seed ROI for CBH was placed in the coronal plane, in middle of the tract as visualized in the parahippocampal gyrus with regions of inclusion and termination at drawn on the coronal plane at the uncal apex in the hippocampal head (anterior) and posterior termination at the inferior aspect of the splenium of the corpus callosum, drawn on the transverse-oriented image. Uncinate fasciculus was determined using a region of inclusion at the external capsule on the coronal plane on the slice in which the temporal lobe and frontal lobe become contiguous with regions of inclusion at the anterior temporal lobe and in the prefrontal lobe. Regions of exclusion were liberally applied to mask out additional streamlines. Fornix tracts were subsequently edited to restrict streamlines to the posterior aspect, covering the crus and posterior body.

Spatial transformation of masks to native space. The spatial transformation matrices produced by DTI-TK during registration to template space were inverted and combined. We sampled the s-form matrix from the original diffusion volume prior to nonlinear registration

and used this information to reorient the deprojected masks from neurological to radiological orientation, and back to the native coordinate space.

Inspection of streamlines. In 18 cases, the rater adjusted the inclusion masks for CBD and CBH, or swapped seed and inclusion masks. Cases with fewer than 15 streamlines were deemed unreliable and treated as missing values. Streamlines for fornix were particularly vulnerable to producing too few streamlines, and cases with less than 15 streamlines in left, right, or bilateral fornix were produced in approximately 10% of the sample. The numbers of cases assigned as missing values, varied by region and hemisphere, and the final totals of cases with missing streamlines were as follows: CBD-left = 8, CBD-right = 8, CBH-left = 16, CBH-right = 23, fornix-left = 31, fornix -right = 44, UF-left = 8, UF-right = 8.

Hippocampal subfield segmentation. We used the Automated Segmentations of Hippocampal Subfields (ASHS; Yushkevich et al., 2015; Yushkevich et al., 2010) software with a customized atlas for HC subfield morphometry (Bender et al., 2018). The customized atlas was built using a modified version of the manual demarcation and tracing rules described previously (Bender et al., 2013; Daugherty et al., 2016), and includes a slightly more lateral placement of the SUB-CA1/2 boundary as a compromise of that boundary placement in different atlases included in commonly used HC subfield segmentation software (Iglesias et al., 2015; Yushkevich et al., 2015). This atlas was built from a lifespan sample, and included data from 10 children and adolescents (age range = 7–13 years; mean age = 10.08, SD = 2.64 years; 50% female), four young adults (age range = 22–24 years; mean age = 23.00, SD = 0.82 years; 50% female), and 14 older adults (age range = 62–78 years; mean age = 69.64, SD = 4.63 years; 50% female). To ensure ASHS demarcation was performed on the full extent of the HC body, we used an extended atlas (Bender et al., 2018). The extended atlas was built from manually demarcated data in which the ranges of inclusion were extended beyond anatomical landmarks normally designated for manual segmentation

procedures. Thus, images included for atlas building by tracing subfields on one to two additional anterior slices and one to two additional posterior slices to the manually defined ranges, depending on visibility of subfields. In anterior slices, any visible tissue from the long digitation of the HC head was not included and demarcation was limited to clearly apparent HC 'body-like' regions on slices anterior to the uncal apex. Automated segmentation failed or produced errors in 36 out of 337 cases (10.68%) included for analysis, and these were treated as missing values in subsequent analyses.

Manual range determination. We separately determined the ranges of slices for inclusion in each HC subfield region of interest (ROI) for left and right hemisphere. The first slice following the uncal apex, and on which the long digitation of HC head was no longer visible and did not exhibit partial volume artifacts served as the anterior limit of HC body. The *penultimate* slice on which the lamina quadrigemina (LQ) was visible served as the posterior limit for inclusion. We allowed for hemispheric differences in posterior range if only left or right LQ was visible on the final slice, including presence of a partial volume effect. Using a custom Bourne shell script, we truncated the output from ASHS to the individualized, manually-determined ranges.

ICV correction. As described previously (see Bender et al., 2013 for a complete description) Standard-space masking was applied to remove non-brain tissue, and a fractional intensity threshold of 0.2 and we used the -A option for the 'betsurf' feature for estimation of skull surfaces (Jenkinson et al., 2005). An experienced operator (ARB) reviewed the results and identified 11 cases in which the procedure produced holes in the ICV brain mask, and filled the holes using tools in ITK-SNAP. We used ICV values sampled from the outer skull mask to adjust HC subfield volumes for head size.

Data Analysis.

Latent growth model (LGM). We specified a model with latent factors for intercept

and slope. For all trials, the factor loadings for the intercept were all fixed at 1. The factor loadings for the 5 trials were estimated using a latent basis free model approach (McArdle, 1986) in which the first and last indicator factor loadings are fixed at 0 and 1, respectively, and the remaining factor loadings are freely estimated.

Brain Parameter Confirmatory Factor Analyses (CFA).

Brain CFAs. All CFA models for HC subfield volumes converged with acceptable fit according to most indices. Initial estimation of the three–factor model showed negative residual variance for the left CA3/DG indicator. We addressed this by fixing the residual variance for this indicator to zero for all subsequent modeling steps, which resulted in unstandardized factor loading of 1 for this indicator. As shown in Table SM1, the standardized factor loadings for the remaining HC subfield factor indicators were estimated between 0.711 (right CA3/DG) and 0.962 (left CA1/2). The comparison of model fit indices for one- and four–factor models showed the four–factor model to provide the best fit (Table SM2). Model fit in the four–factor model was improved by specifying covariances between indicators for subfields within each hemisphere. The four–factor model showed significant associations between all HC subfield factors, ranging from moderate to strong.

Initially, for both HC subfield volumes and DTI tracts, we compared the model fit of two different approaches: (1) separate latent factors per region or tract with the correlations between latent factors freely estimated, and (2) all indicators loading onto a single factor (SM Fig. 2 similar to a first principle component). For both HC subfield volumes and each WM measure, we assessed which measurement model (individual latent factor or single factor) best fit the data.

Comparison of model fit for the WM factor models showed poor fit by the one-factor model, and excellent fit by each of the four–factor models (see Table SM2).

Results

Intra-domain brain associations. Consistent with our expectations that factors within the respective domains (i.e., WM or HC subfield) would be highly correlated, we observed significant associations between all HC subfield factors, and between all WM factors for FA, (Table SM2).

References

Bender AR, Keresztes A, Bodammer NC, Shing YL, Werkle-Bergner M, Daugherty AM, Yu Q, Kuhn S, Lindenberger U, Raz N. 2018. Optimization and validation of automated hippocampal subfield segmentation across the lifespan. Hum Brain Mapp. 39:916–931.

Bender AR, Daugherty AM, Raz N. 2013. Vascular Risk Moderates Associations between Hippocampal Subfield Volumes and Memory. J Cognitive Neuroscience. 25:1851–1862.

Daugherty AM, Bender AR, Raz N, Ofen N. 2016. Age differences in hippocampal subfield volumes from childhood to late adulthood. Hippocampus. 26:220–228.

Iglesias JE, Augustinack JC, Nguyen K, Player CM, Player A, Wright M, Roy N, Frosch MP, McKee AC, Wald LL, Fischl B, Van Leemput K, Initiative FTADN. 2015. A computational atlas of the hippocampal formation using ex vivo, ultra-high resolution MRI: Application to adaptive segmentation of in vivo MRI. NeuroImage. 115:117–137.

Jenkinson M, Pechaud M, Smith S. 2005. BET2: MR-based estimation of brain, skull and scalp surfaces. In:. Presented at the Eleventh annual meeting of the organization for human brain mapping. Toronto. p. 167.

Yushkevich PA, Pluta JB, Wang H, Xie L, Ding SL, Gertje EC, Mancuso L, Kliot D, Das SR, Wolk DA. 2014. Automated volumetry and regional thickness analysis of hippocampal subfields and medial temporal cortical structures in mild cognitive impairment. Hum Brain Mapp. 36:258–287.

Yushkevich PA, Wang H, Pluta J, Das SR, Craige C, Avants BB, Weiner MW, Mueller S. 2010. Nearly automatic segmentation of hippocampal subfields in in vivo focal T2-weighted MRI. NeuroImage. 53:1208–1224.

Table SM1. Standardized factor loadings from single-factor latent models

	Left	Right
HC Subfield		
SUB	0.918	0.698
CA1/2	0.962	0.714
CA3/DG	0.998	0.711
FA		
CBD	0.902	0.825
CBH	0.785	0.920
Fornix	0.783	0.416
UF	0.827	0.776

Notes: SUB – subiculum; CA1/2 – aggregated ROI for CA1 and CA2 subfields; CA3/DG – aggregated ROI for CA3 and DG; CBD – dorsal cingulum bundle; CBH – hippocampal cingulum bundle; UF – uncinate fasciculus; FA – fractional anisotropy

Table SM2. Goodness of Fit Statistics for CFAs and Covariance Models

Model	χ^2(df)	*p*	χ^2/df	CFI	RMSEA	RMSEA 90% CI	SRMR
Verbal Learning Memory Test (VLMT) LGM							
Linear slope	182.129 (10)	.000	18.213	0.839	0.226	0.039–0.120	0.130
Latent basis	42.554 (7)	.000	6.079	0.967	0.123	0.089–0.159	0.074
HC Subfield Volume							
1-Factor	279.547 (6)	.000	46.591	0.791	0.389	0.351–0.429	0.064
3-Factor	3.563 (4)	.468	0.891	1.000	0.000	0.000–0.083	0.020
DTI - FA							
1-Factor	288.511 (20)	.000	14.426	0.704	0.202	0.181–0.223	0.086
4-Factor	9.437 (14)	.802	0.674	1.000	0.000	0.000–0.035	0.013
Combined Model							
HC-WM	156.026 (136)	.115	1.147	0.994	0.021	0.000-0.035	0.030
HC-WM-Covs‡	199.518 (150)	.004	1.330	0.985	0.031	0.018-0.042	0.036
Second-order factor model							
Covariances only	171.26 (119)	.001	1.439	0.984	0.036	0.023–0.048	0.043

Notes: ‡: Covariate model including direct paths to each latent factor from observed covariates: participant years of age and educational attainment (centered at sample mean) and sex.

Table SM3. Comparison of factor loadings in latent growth models

	Factor Loadings by VLMT Trial					Model Fit		
Model	1	2	3	4	5	RMSEA	CFI	SRMR
Latent Basis Model*	0.000	0.452	0.698	0.889	1.000	0.118	0.961	0.097
Linear Slope	0.000	1.000	2.000	3.000	4.000	0.238	0.839	0.139

Notes: Latent basis model = Factor loadings for trial 1 fixed to 0 and for trial 5 fixed to 1, and all other loadings are freely estimated. Note that the difference in the last factor loading between models merely reflects a rescaling of the latent slope variable but does not affect model fit. * indicates factor loadings used in subsequent modeling steps.

Table SM4. Significant associations between parameters within brain domain

	Association	Estimate	S.E.	*p*	95% CI
HC Subfields					
	CA1/2↔SUB	0.649	0.042	.000	0.560–0.734
	CA3/DG↔SUB	0.629	0.040	.000	0.548–0.705
	CA3/DG↔CA1/2	0.820	0.024	.000	0.771–0.864
WM fractional anisotropy (FA)					
	CBH↔CBD	0.554	0.050	.000	0.460–0.639
	Fornix↔CBD	0.223	0.080	.005	0.059–0.408
	Fornix↔CBH	0.365	0.090	.000	0.166–0.578
	UF↔CBD	0.552	0.051	.000	0.450–0.645
	UF↔CBH	0.585	0.051	.000	0.445–0.690
	UF↔Fornix	0.303	0.087	.000	0.100–0.513

Notes. SUB = subiculum, CBD = dorsal cingulum bundle, CBH = hippocampal cingulum bundle, UF = uncinate fasciculus.

Table SM5. Fit indices for 2nd order models without latent interactions

Model	χ2 (df)	χ2 / df	*p*-value	CFI	RMSEA	SRMR
No Covariates	221.776 (144)	1.54	.000	0.977	0.040	0.051
Age	250.185 (161)	1.55	.000	0.974	0.041	0.051
Age, Sex	299.782 (176)	1.70	.000	0.964	0.046	0.053
Age, Sex, Edu	309.887 (191)	1.62	.000	0.959	0.042	0.052

Notes: Results shown for reduced model, specified without latent intercept factor as a dependent variable.

Table SM6.

Model	*LL-Orig*	*LL-LI*	*LLR*
No Covariates	-530.08	-527.19	5.776*
Age	-502.81	-500.04	5.524*
Age, Sex	-501.78	-499.15	5.258*
Age, Sex, Edu	-1241.20	-1238.50	5.404*

Notes: LL: log-likelihood value. Orig: Original model without latent interaction. LI: Latent moderated structural equation model specifying the interaction between second order factors for hippocampal volume and limbic white matter fractional anisotropy. LLR: Log-likelihood ratio test, a two-tailed test of differences in fit. LLR statistic shows significant differences between models including latent interaction and those that do not, with lower log-likelihood indicating better fit.

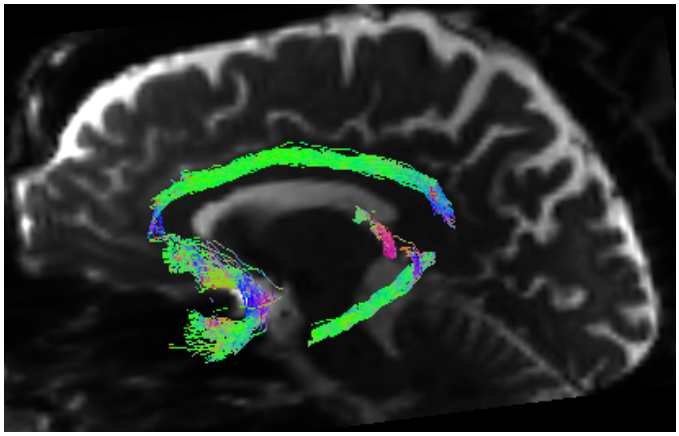

Figure SM1. Illustration of constrained spherical deconvolution diffusion tractography using MRtrix3. Using deterministic fiber tractography we sampled free water-corrected fractional anisotropy from streamlines representing canonical limbic system white matter fiber tracts: uncinate fasciculus, dorsal and parahippocampal cingulum bundle, and posterior fornix.

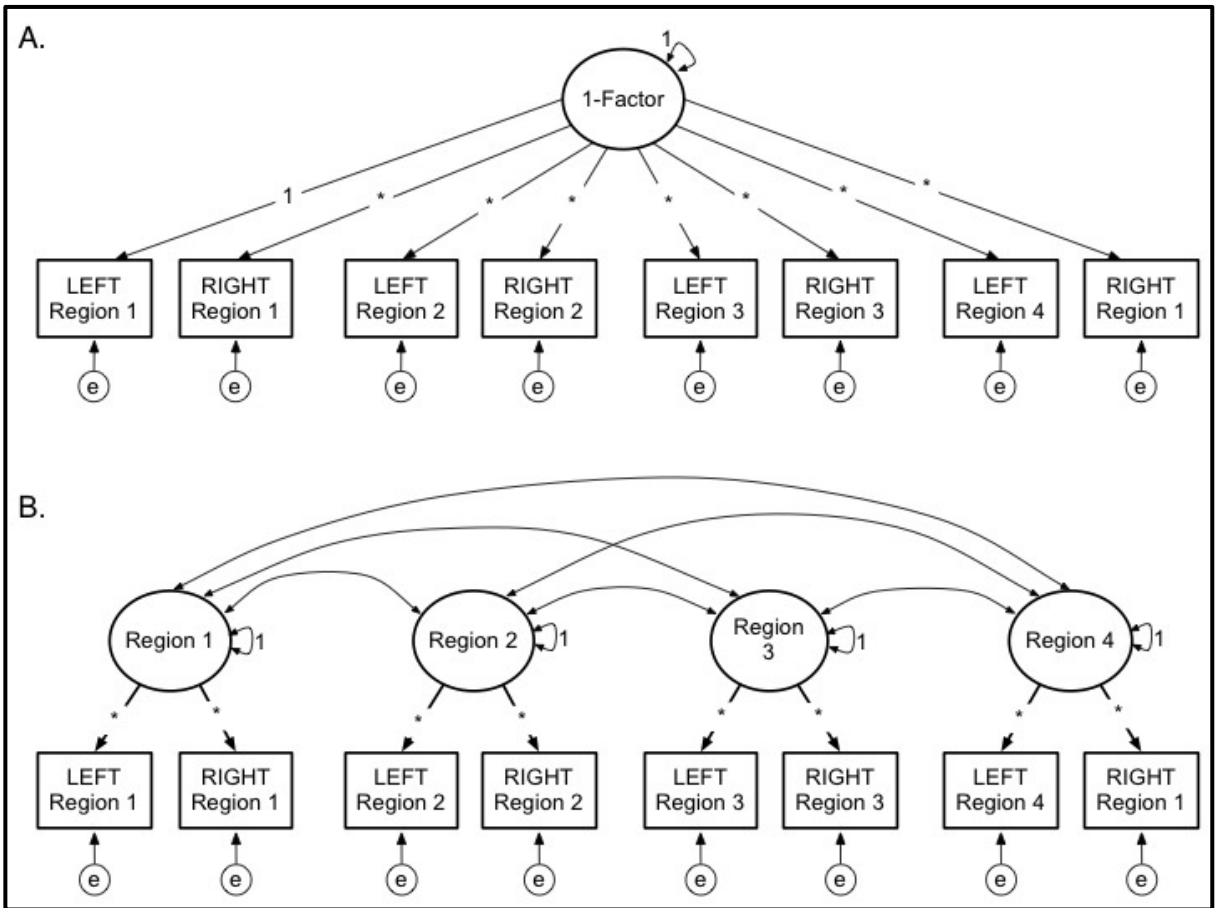

Figure SM2. Alternative measurement models for DTI parameters and hippocampal subfields. A. One-factor model with all indicators loading onto a single factor. B. Four-factor model, with dual indicators representing left and right hemispheres for each latent factor representing individual, bilateral anatomical regions (i.e., WM tract or HC subfield volume).

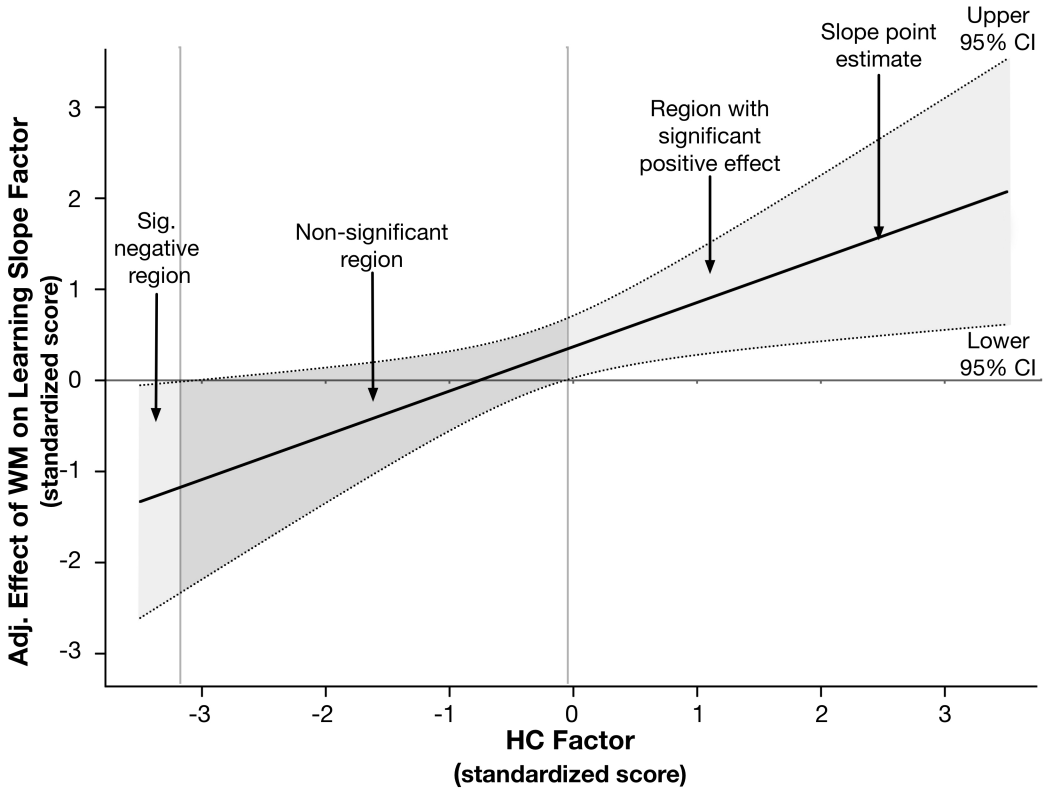

Figure SM3. Johnson-Neyman plot illustrating the decomposed interaction to test the moderating effect of hippocampal volume (HC) on the effect of limbic white matter (WM) fractional anisotropy on the verbal learning slope latent factor. The x-axis represents the continuous moderator – here, the standardized HC factor score, and the y-axis represents the effect of the WM latent factor in the latent interaction on the verbal learning slope parameter, adjusted for other model parameters. The solid regression line reflects the association between the adjusted effect of the WM factor on the learning slope latent factor, as a function of level in the HC factor. The dotted lines represent the upper and lower 95% confidence band around the regression slope. The solid horizontal line at y=0, and the dotted vertical line at x=0 are superimposed to assist with interpretation. Regions where the confidence bands overlap with y=0 indicates the levels of the x-variable in which the effect represented by the regression slope are not significant. The confidence bands overlap with zero until the HC factor score is slightly greater than 0, demonstrating that the adjusted effect of WM volume on learning is only apparent at non-negative values of the HC factor.